PODAR: Modeling Driver's Perceived Risk with Situation Awareness Theory

Chen Chen, Zhiqian Lan, Guojian Zhan, Yao Lyu, Bingbing Nie, Shengbo Eben Li*

Corresponding Author: Shengbo Eben Li, lishbo@tsinghua.edu.cn

ABSTRACT

Proper estimation of driver perceived risk is the key to designing human-like planning and control algorithms for autonomous vehicles to generate human-like behaviors and gain people's trust. By introducing human situation awareness theory, this paper proposes a concise, effective, and general-scenarios applicable model, termed Potential Damage Risk (PODAR), to estimate perceived risk during driving. PODAR consists of two components: potential damage and attenuation functions, corresponding to the "uncertainty" and "adverse consequences" in risk definition. Trajectories prediction for both the host and surrounding objects are applied first to obey the situation awareness theory, and the potential damage is calculated at each predictive timestep by assuming a virtual collision. Then temporal and spatial attenuation functions are used to transfer damages to risk. Numerical tests under typical driving situations, including side passes, car-following, and conflicts, have proved that PODAR can provide rational risks consistent with human cognition.

* Codes for PODAR can be found here: https://github.com/ChenChenGith/PODAR

Keywords: perceived risk, driving safety, situation awareness, collision damage, human-like

1 Introduction

Autonomous vehicles provide a promising solution to road safety and traffic congestion problems worldwide [1][2]. However, before fully autonomous vehicles (SAE Level 5) can be widely deployed, it will be a long term that humans need to be involved in driving tasks [3]. Getting people's trust is the key to building a friendly environment in self-driving development. Research has shown that if an automated vehicle performs unexpected actions, making drivers feel dangerous, it will lose human trust and be taken over control, even be rejected from use [4]. Therefore, it is significant to model driver perceived risks, supporting the vehicle planning and control algorithms to output human-like behaviors.

Risk is generally defined as the "likelihood and severity of hazardous events" [5][6], which is generally used in theories of human choice like consumer choice [7], financial management [8], and insurance design [9]. Two critical dimensions in the risk concept are "uncertainty" and "adverse consequence" [10], and for driving risk, they could be regarded as the probabilities and damages of collisions correspondingly. More profoundly, risk is people's subjective judgment according to current environments. Therefore, it can also be explained by the human situation awareness (SA) theory [11]. Endsley [11] divides human SA into three levels: Lv1-Perception: detecting surrounding basic information; Lv2-Comprehension: integrating multiple information and determining relevance to the goal; Lv3-Projection: forecasting situation events and dynamics in the near future. If setting the situation awareness goal as driving risk estimation, Lv2 SA can approximately correspond to "consequence/damage", i.e., the estimated potential collision damages brought from different objects. Lv3 SA can be regarded as "uncertainty/probability" because only un-happened collisions can be called risk, where risk is taken as the projection of potential damage. Fig. 1 shows a sketch of the SA theory's relationship in perceiving driving risk.

Some measures have been proposed to estimate driving risks (Fig. 1). Time-to-collision (TTC) [13] series, including its variants like Time Exposed Time-to-collision (TET) [14], Time Integrated Time-to-collision (TIT) [14], Deceleration Rate to Avoid a Crash (DRAC) [15][16], are widely used in estimating longitudinal behavior of vehicles. Advanced modification like Post-Encroachment Time (PET) [17][18], Time-to-lane-crossing (TLC) [19][20] can further handle lateral movements. TTC-series measures predict trajectories for both host and surrounding objects with a constant speed assumption, and the "uncertainty" is estimated by the remaining time until a collision or needed deceleration to avoid the collision. However, one common drawback is that they concentrate on the happening of collision events instead of collision "consequences." Besides, the situation-specific risk assessment needs prior knowledge for scenario classification and is inconvenient for comparison.

Recent years, field theory is introduced into driving risk estimation to adapt to multiple scenarios. Safety field (SF) [21][22] considers the superposition of the potential field, kinetic field, and behavior field to get a risk map, as shown in Fig. 1. The "consequence" is estimated by the virtual mass of objects, and the "uncertainty" is estimated by three factors: a distance-related coefficient, a speed and angle-related exponent coefficient, and a behavior related coefficient DR. SF considers object dynamics only via the relative speed value in the kinetic field and ignores host vehicle states. Thus, SF seems to provide just a "nearly" static risk map of the current situation, making it unable to deal with risks brought from future potential collisions.

On the contrary, Driver's Risk Field (DRF) [23][24] estimates perceived risk by modeling the region in front of the host vehicle as a representation of "uncertainty" (Fig. 1). A parabola and several Gaussian functions are used for longitudinal and lateral direction, generating a 3D mesh indicating drivers' subjective belief about the probability of event occurrences (Fig. 1). The "consequence" is held constant by assigning different values to different obstacle types. The parabola function along the driving direction could be regarded as a prediction of host vehicle motion ("uncertainty"), while dynamics of surrounding objects are ignored. The ignorance breaks the SA theory and would lead to improper risk estimation of future potential collisions, similar to SF.

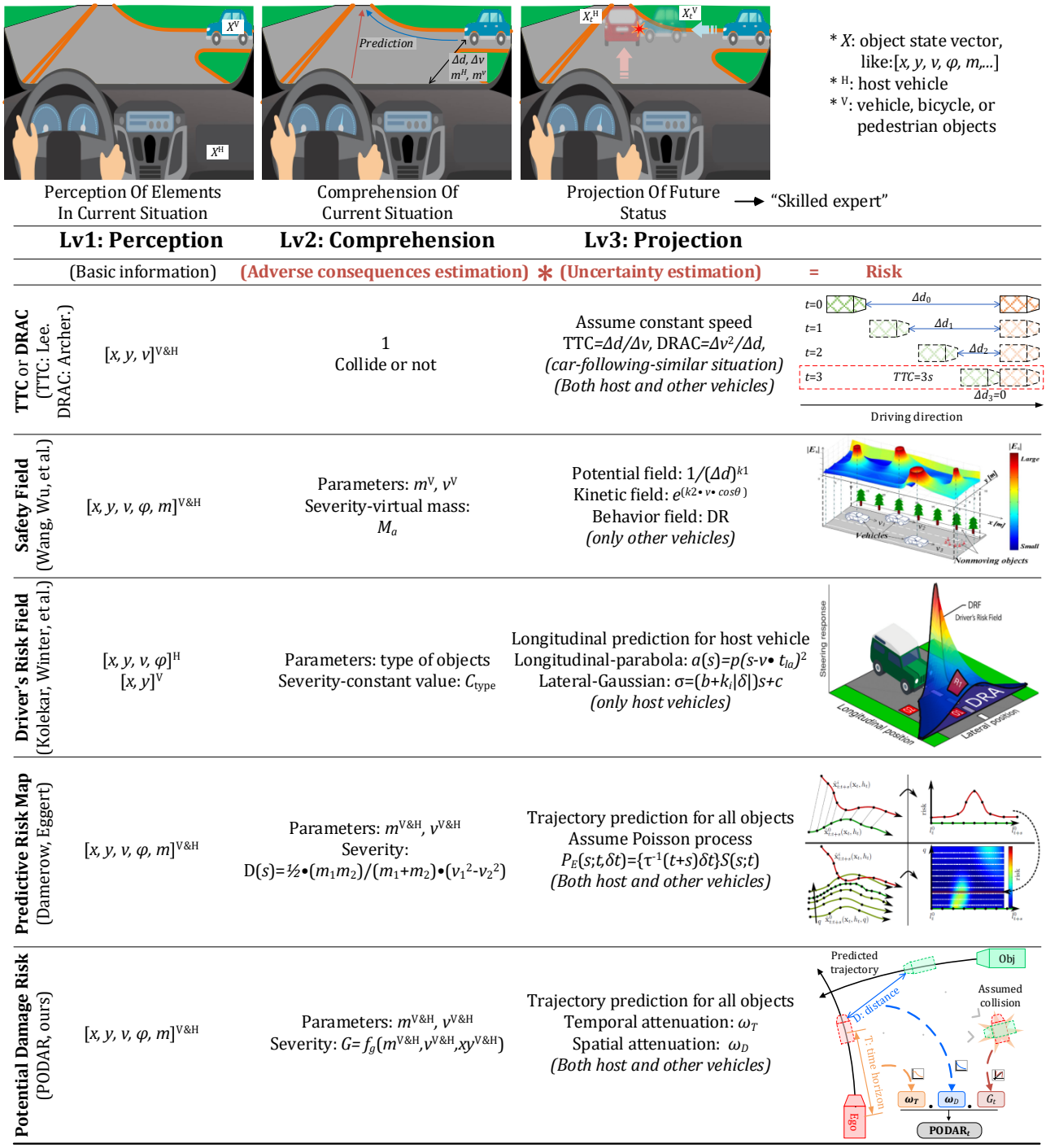

Fig. 1. Levels of SA and analysis of typical driving risk measures

In the SA theory, Endsley [12] emphasizes that the Projection (Lv3) is the mark of a skilled expert, and the host and surrounding vehicle motion are both essential for risk estimation in the dynamic driving system. However, existed driving risk measures mentioned above miss some components: SF, DRF only model one of host and surrounding object motions, and TTC-series omits the "consequence". Additionally, since field-based measures always utilize the product of consequence and uncertainty based on grid discretization to get a scalar value representing driving risk, they are suffering

high computational complexity. It could be a significant cause why SF and DRF only handle one of the fields for a host-object pair instead of superimposing two fields. The complexity also increases the application difficulty for self-driving online planning.

Common sense is that human attention is finite. Some eye gaze-related studies [26][27] and public datasets [28][29] have shown a phenomenon that drivers always pay their attention to a few key objects instead of distributing attention evenly to the front region. One method named Predictive Risk Maps (PRM) predicts future trajectories of both host and surrounding vehicles and uses pairwise states at the same predictive timestep to estimate risks during the prediction horizon. A kinetic energy-like form is used for collision "consequence" estimation, and a Poisson process is used to estimate the "uncertainty" at each predicted time. However, no scalar value indicating current driving risk is provided but a risk map is generated by adopting different prediction parameters (Fig. 1) at each timestep, which implies high computation loads. The non-scalar estimation also prevents its application to most trajectory planning algorithms that need a cost value in their optimization process.

Based on the SA theory and the definition of driving risk, this paper proposes a Potential Damage Risk (PODAR) model that estimates the perceived risk in a scalar value. Similar to PRM, PODAR contains predictions of both the host and surrounding vehicles. A virtual collision is assumed for each predictive timestep to get the "consequence," termed as potential damage. For "uncertainty", instead of using probabilities like DRA and PRM, a more intuitionistic method, which adopts two attenuation functions from spatial and temporal dimensionalities to approximate probability, is used to transfer damage values to risks (Fig. 1). The perceived risks can be estimated by combining the "consequence" and "uncertainty." The proposed model is proven to be able to get driving risks similar to human cognition under all the typical driving situations via case studies, while current measures mentioned above cannot adapt to some scenes.

2 Methods

2.1 PODAR Model

As mentioned in the Introduction, we approximately correspond Lv2 SA to "consequence/damage" and Lv3 SA to "uncertainty/probability" of risk. SA theory [12] suggests that time is a strong part of Lv2 SA and Lv3 SA. Here, "consequence" is extended to the prediction horizon by estimating the damages of assumed collisions using the predicted states of the host vehicle and surrounding objects.

Although the risk is always defined as the "likelihood and severity of hazardous events", we suggest a more intuitive description that risk is the threat of possible damage, implying an assumption that damage is the supremum of risk. The risk value should collapse to the damage value when hazardous events occur. In this case, we resolve the "uncertainty" into two attenuation functions from temporal and spatial dimensionalities, where the temporal aspect describes the remaining time due to prediction, and the spatial aspect describes the uncertainty brought from the remaining distance between vehicles at each predictive timestep.

With this concept, PODAR first predicts the future trajectories of both the host vehicle and surrounding objects. Then, at each predictive timestep, a virtual collision is assumed and results in potential damage G. Next, two attenuation functions, ω_D and ω_T that respectively represent spatial and temporal dimensionalities, are superposed to potential damage, deriving the perceived risk values. Finally, since there are multiple objects and prediction steps, the maximum risk value is determined as the final driving risk to simulate human's finite attention.

2.1.1 General structure

A general structure of the PODAR model, which suggests driving risk to be the attenuation from potential collision damage, is proposed as Equation (1) (Fig. 2).

$$\mathrm{PODAR} = \max_{t,n} \left\{ \mathrm{PODAR}_t^n \right\} \tag{1}$$

$$\mathrm{PODAR}_t^n = G_t^n \cdot \omega_D \cdot \omega_T \tag{2}$$

$$t \in \{0,1,\ldots,T\}, n \in \{1,\ldots,N\}$$

where,

PODAR = final driving risk;
t = timestep in prediction horizon;
T = prediction horizon;
n = index of surrounding object (including motor vehicle, pedestrian, bicycle);
N = numbers of surrounding objects;
PODAR_t^n = driving risk from the n-th object at timestep t;
G_t^n = potential collision damage from the n-th object at timestep t;
ω_D = spatial attenuation coefficient related to distance;
ω_T = temporal attenuation coefficient related to time.

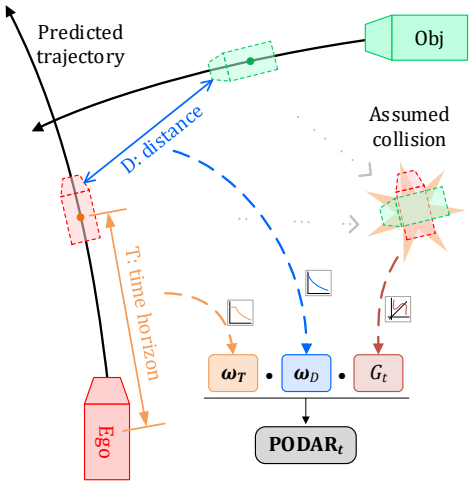

Fig. 2. PODAR structure

2.1.2 Potential damage

It is assumed that at each predictive timestep, the host vehicle and the surrounding object have a virtual collision with their states at that time. Thus, the potential damage can be formulated by Equation (3):

$$G_t^n = f_g\left(\boldsymbol{v}_t^{\text{host}}, \boldsymbol{v}_t^n, \boldsymbol{p}_t^{\text{host}}, \boldsymbol{p}_t^n, M^{\text{host}}, M^n\right) \tag{3}$$

where,

f_g = function for estimating potential collision damage;
$\boldsymbol{v}_t^{\text{host}}$ = velocity vector of the host vehicle at timestep t;
$\boldsymbol{v}_t^n$ = velocity vector of the n-th object at timestep t;
$\boldsymbol{p}_t^{\text{host}}$ = position vector of the host vehicle at timestep t;
$\boldsymbol{p}_t^n$ = position vector of the n-th object at timestep t;
M^{host} = virtual mass of the host vehicle;
M^j = virtual mass of the n-th object.

An empirical model that uses a kinetic energy-like form is provided for practicability, as shown in Equations (4)-(6). This form has a physical implication of kinetic energy that can describe the collision's severity and is used in some driving risk studies [30][31]. However, instead of directly using speed values, an integrated representation of host and target object velocities (V_t), which includes two parts, velocity differential (delta-v, the first part in Equation (5)) and speed magnitude (the second part in Equation (5)), is used in our model. The velocity differential is an acknowledged measure of the severity of a crash and has been used in many studies [32][33]. The speed magnitude is also an essential factor, acting as a supplement to the velocity differential. Generally, higher speeds will cause more damage even if the relative speeds are the same. Weights α and $(1-\alpha)$ are assigned to velocity differential and magnitude, respectively, to balance their contribution to the estimated damage.

$$G_t = \frac{1}{2} \cdot \left(M^{\text{host}} + M^n\right) \cdot V_t \cdot |V_t| \tag{4}$$

$$V_t = \alpha \cdot \left\langle \boldsymbol{v}_t^n - \boldsymbol{v}_t^{\text{host}}, \frac{\boldsymbol{p}_t^{\text{host}} - \boldsymbol{p}_t^n}{\left|\boldsymbol{p}_t^{\text{host}} - \boldsymbol{p}_t^n\right|} \right\rangle + (1-\alpha) \cdot \left(\left|\boldsymbol{v}_t^n\right| + \left|\boldsymbol{v}_t^{\text{host}}\right|\right) \tag{5}$$

$$M = m \cdot s \tag{6}$$

where,

V_t = integrated representation of host and target object velocities;
α = weight for balancing velocity differential and magnitude;
m = actual mass of the host vehicle or the surrounding object;
s = damage sensitivities for different object types.

The velocity differential is calculated using the inner product of the relative velocity vector and the normalized relative position vector instead of directly using the relative speed value to treat different scenes, as shown in Fig. 3a. The five surrounding vehicles have the same relative velocity vector $d\boldsymbol{v}$, resulting in the same relative speed value $|d\boldsymbol{v}|$. Meanwhile, objects 1, 2, and 5 are approaching the host vehicle, and objects 3 and 4 are running away from the host vehicle. Intuitively, objects 1, 2, and 5 should be more dangerous than objects 3 and 4. However, their risks will be the same if one uses the relative speed value rather than the velocity differential $|\Delta\boldsymbol{v}|$ to form the integrated representation V_t. It is easy to imagine that this design is also suitable for the car-following situation, which will result in the same relative speed values used in TTC.

It should be noted that the inner product will be negative when the intersection angle is larger than $\pi/2$. Critical situations are when one object has not passed the host vehicle entirely, as shown in Fig. 3b. To deal with this problem, two inner products using $\Delta \boldsymbol{p}_f$ and $\Delta \boldsymbol{p}_r$, which are determined by the object's rear bumper center point and the host vehicle's front/rear bumper center points, are calculated. The maximum value between the two inner products is finally used to form the integrated representation V_t.

There is a normalization $\left(\boldsymbol{p}_t^n - \boldsymbol{p}_t^{\text{host}}\right)/\left|\boldsymbol{p}_t^n - \boldsymbol{p}_t^{\text{host}}\right|$ because the inner product of the relative velocity vector and the relative position vector is expected only to describe the velocity differential. Spatial attenuation function ω_D will handle the effects of distance.

The virtual mass M is determined as the product of the actual mass m and the injury sensitivity s for different objects. For example, vehicles have greater mass and higher kinetic energy than pedestrians or bicycles. However, vehicles have many security measures like safety belts, helping prevent occupants' injury, while pedestrians will suffer enormous harm. Thus, coefficients describing damage sensitivity are multiplied to m to emphasize the importance of some vulnerable participants.

A form of $1/2 \cdot m \cdot V_t \cdot |V_t|$ is used instead of directly using $1/2 \cdot m \cdot V_t^2$ because the kinetic energy is a scalar, while the V_t calculated by the inner product would get negative values. This form can reflect the potential damages, especially when objects are driving away from the host vehicle.

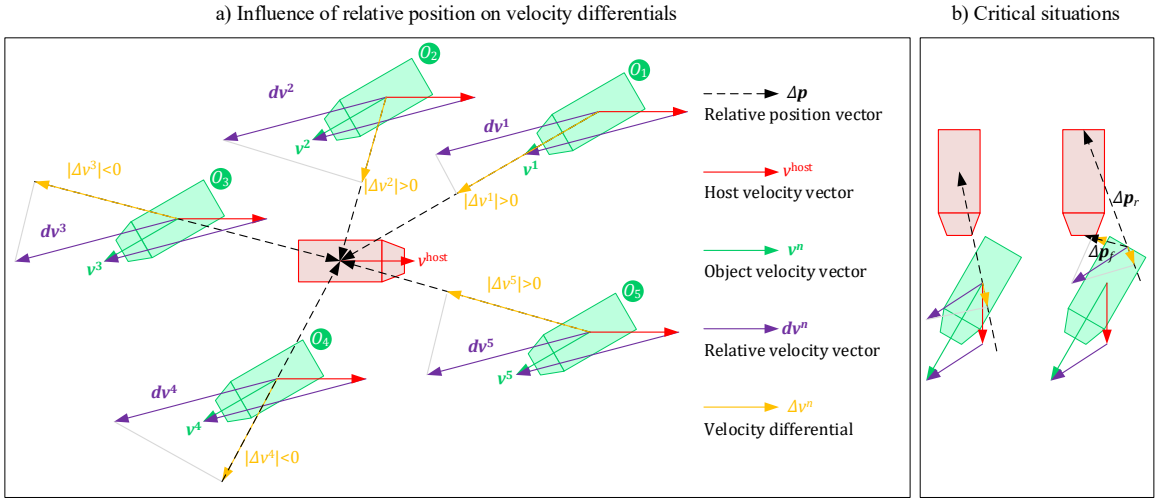

Fig. 3. Velocity differentials under different conflict situations

2.1.3 Attenuation

PODAR suggests that risk comes from the attenuation of potential damage since there is time and room for the driver's response [34]. Thus, both spatial and temporal dimensionalities are modeled, although they are not easy to be separated because the relative distance will change as time goes by. However, only using one of the two dimensionalities can not fully describe the uncertainty. DRF [23] also separates spatial and temporal dimensionalities by considering longitudinal and lateral directions.

The attenuation functions in PODAR for spatial and temporal dimensionalities should meet Equation(7). When a collision occurs, i.e., distance=0 and time=0, risk collapses to the damage. When a collision is predicted in a future timestep, i.e., distance=0 and time≠0, the attenuation only comes from the temporal dimensionality. When distance≠0 and time=0, it means the current moment, and the attenuation only comes from the spatial dimensionality.

$$\begin{aligned} &\omega(\cdot) = \omega_D(d) \text{ or } \omega_T(t) \\ \text{s.t.} \quad &\omega(0) = 1 \\ &\omega(x_1) \geq \omega(x_2), \forall x_1 \leq x_2 \end{aligned} \tag{7}$$

where,

d = the relative contour distance between the host vehicle and the surrounding object.

For practicability, empirical models for ω_D and ω_T are provided here. Two reciprocal functions are used to model ω_T and ω_D, as shown in Equations (8) and (9). Parameters A and B are used to adapt the attenuation curves as shown in Fig. 4. The emergency braking time (T_{EB}) are considered in time attenuation based on an assumption that potential damages will not attenuate before the host can entirely stop.

$$\omega_T = \begin{cases} 1, & t \leq T_{\text{EB}} \\ \dfrac{A}{t - T_{\text{EB}} + A}, & \text{else} \end{cases} \tag{8}$$

$$\omega_D = \begin{cases} 1, & d \le 0 \\ \dfrac{B}{d+B}, & d > 0 \end{cases} \tag{9}$$

where,

T_{EB} = the emergency braking time of the host vehicle.

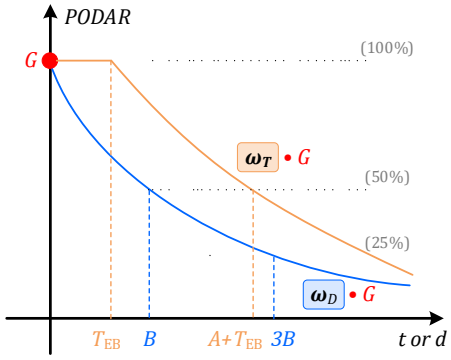

Fig. 4. Attenuation curve of ω_T and ω_D

2.1.4 Treatment of negative values

Potential collision damage G might be negative when objects are moving away from the host vehicle, as the objects 3 and 4 in Fig. 3a. Directly using the product of negative damage and attenuation coefficient is not proper as it will let the risk value increase inversely. Here, we introduce a trick to deal with these situations. If G gets negative values among all the prediction horizons, an inverse-attenuation is adapted, as seen in Equation (10). Then still, the maximum value of all PODAR_t^n is used as final driving risk.

$$\mathrm{PODAR}_t = \begin{cases} G_t \cdot \omega_D \cdot \omega_T & \exists G \ge 0 \\ G_t \cdot (1 + (1 - \omega_D \cdot \omega_T)) & \forall G < 0 \end{cases} \tag{10}$$

2.2 Cases study settings

To verify the feasibility, PODAR is tested in several typical driving scenarios by numerical simulation. First, a set of empirical parameters used in PODAR model is provided. Then two classes of situations, driving with single and multiple surrounding objects, are designed to test the performances of PODAR. A comparison of scene applicability between PODAR and currently existing measures, including TTC, DRAC, SF, and DRF, will be shown in the Results section.

2.2.1 Model detail

Model Parameters.

α in Equation (5) is set as 0.7, which is determined by several simulation tests to balance the significance of velocity differential and speed magnitude. A in ω_T is set as 1 second, which means that damage will attenuate to 50% at $1 + T_{\mathrm{EB}}$ seconds. B in ω_D is set as 2.5 meters, meaning damage will attenuate to 25% when the relative distance is 7.5 meters. The actual mass m of passenger car, truck, bicycle, and pedestrian are set as 1.8, 4.5, 0.09, and 0.07 *tons* according to actual average mass values [35][36][37], respectively. The damage sensitivity s for passenger cars and trucks are set as 1; for bicycles and pedestrians are set as 50 to emphasize their importance beyond passenger cars. Finally, a coefficient of 0.02 is multiplied to PODAR to scale the values in a proper range.

Trajectory prediction.

Accurate trajectory prediction is a hot topic, especially in the decision-making and control of autonomous vehicles, and is also essential for driving risk assessment. Neural networks are powerful in dealing with the interaction among traffic participants and provide high-accurate prediction results [38][39][40]. An accurate prediction model is excellent but brings a high computing load and needs tremendous effort in model training. One literature [41] mentions that a simple constant velocity model can achieve reasonable performance in predicting pedestrians' motion. Although it is not a vehicle-based conclusion, we suggest that a similar concise model can be used in our study based on the consideration that pedestrian motions are more stochastic than vehicles.

For simplicity, a constant acceleration-yaw rate model is used in the trajectory prediction, as shown in Equation (11). The prediction horizon is 3 seconds. Fig. 5 shows the sketch of the trajectory prediction. The Kinematic equations of the model are:

$$\begin{bmatrix} \boldsymbol{p}_{t+1} \\ \boldsymbol{v}_{t+1} \\ \boldsymbol{a}_{t+1} \end{bmatrix} = \begin{bmatrix} 1 & \Delta t & (\Delta t)^2/2 \\ 0 & 1 & \Delta t \\ 0 & 0 & \boldsymbol{A} \end{bmatrix} \begin{bmatrix} \boldsymbol{p}_t \\ \boldsymbol{v}_t \\ \boldsymbol{a}_t \end{bmatrix}$$
$$\text{s.t.} \quad \boldsymbol{A} = \begin{bmatrix} \cos\varphi_0 & -\sin\varphi_0 \\ \sin\varphi_0 & \cos\varphi_0 \end{bmatrix} \tag{11}$$
$$\boldsymbol{p}_{t=0} = \boldsymbol{p}_0$$
$$\boldsymbol{v}_{t=0} = \boldsymbol{v}_0$$
$$\boldsymbol{a}_{t=0} = \boldsymbol{a}_0$$

where,

$\boldsymbol{a}_t$ = acceleration vector (a_x,a_y) at timestep t;
$\boldsymbol{p}_0$ = present position vector;
$\boldsymbol{v}_0$ = present velocity vector;
$\boldsymbol{a}_0$ = present acceleration vector;
φ_0 = present yaw rate.

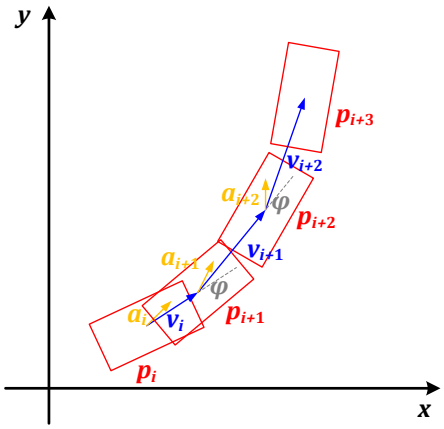

Fig. 5. Sketch of the constant acceleration-yaw rate model

2.2.2 Cases design

Several typical driving situations are designed, including two classes: single object (Fig. 6a-d) and multiple objects (Fig. 6e). The former is to test the rationality of PODAR under different conflict or non-conflict scenes, and the latter is to test the performance of PODAR in general traffic scenarios with multiple traffic participants.

Fig. 6a shows a side pass scene where the host vehicle keeps still, and a vehicle passes it by the right lane. No potential conflict exists within their courses. The initial position of the host vehicle is $\boldsymbol{p}_0^{\text{host}} = (0,0)$, and the surrounding vehicle drives from the initial position of $\boldsymbol{p}_0^{\text{surr}} = (3.5, -25)$ with velocity of 30km/h: $\boldsymbol{v}_0^{\text{surr}} = (0, 30/3.6)$ heading north. This situation lasts for 6 seconds, and performance of PODAR at five key time steps, i.e., $\{0.0, 1.8, 3.0, 4.2, 6.0\}s$, will be shown.

Fig. 6b shows the car-following scenes, including two conditions: (b1) the host vehicle follows, and (b2) the host is the preceding vehicle. The initial position and velocity of the host vehicle is $\boldsymbol{p}_0^{\text{host}} = (0,0)$ and $\boldsymbol{v}^{\text{host}}_0 = (30/3.6,0)$, and the host vehicle is heading east ($\varphi = 0$). The relative distance from the surrounding vehicle to the host vehicle is set as $\pm 10m$ and the speed values of surrounding vehicles are set as $|\boldsymbol{v}_0^{\text{surr}}| = \{15, 20, 30, 45\}km/h$, resulting in total 8 cases. It should be noted that only instantaneous PODAR values of these 8 cases are examined. Besides, a typical car-following process that contains several acceleration-deceleration phases within about 11 seconds is designed. Based on this scene, performances of measures including PODAR, TTC, DRAC, SF, and DRF will be analyzed and compared.

Fig. 6c and Fig. 6d show typical collision cases with seven conflict angles $\phi \in \left\{-\frac{\pi}{4}, 0, \frac{\pi}{4}, \frac{\pi}{2}, \frac{3\pi}{4}, \pi, -\frac{3\pi}{4}\right\}$, where situations c and d differ in the state of the host vehicle. In situation c, the host vehicle stands still at $\boldsymbol{p}_0^{\text{host}} = (0,0)$ while, in situation d, it drives from $\boldsymbol{p}_0^{\text{host}} = (0, -25)$ with velocity of $\boldsymbol{v}_0^{\text{host}} = (0,30/3.6)$. Two speed values of $|\boldsymbol{v}_0^{\text{surr}}| = \{30, 45\}km/h$ and three initial distance values to the coordinate origin of D=$\{15, 25, 35\}m$ are set to surrounding vehicles. Since $25m$ is the exact distance that a vehicle drives through within 3 seconds (trajectory prediction horizon) under 30 km/h, selection of the abovementioned three initial distance values results in three predicted relative motions: pass, just-collide, and not-reach. Additionally, based on situation d, different objects, including trucks, and bicycles, are assigned to test the utility of virtual mass.

Fig. 6e shows a typical right-angle intersection, where traffics are generated by SUMO [42]. A random vehicle is chosen as the host vehicle, driving from south to west. The performance of PODAR will be tested in such scenarios with multi-surrounding vehicles.

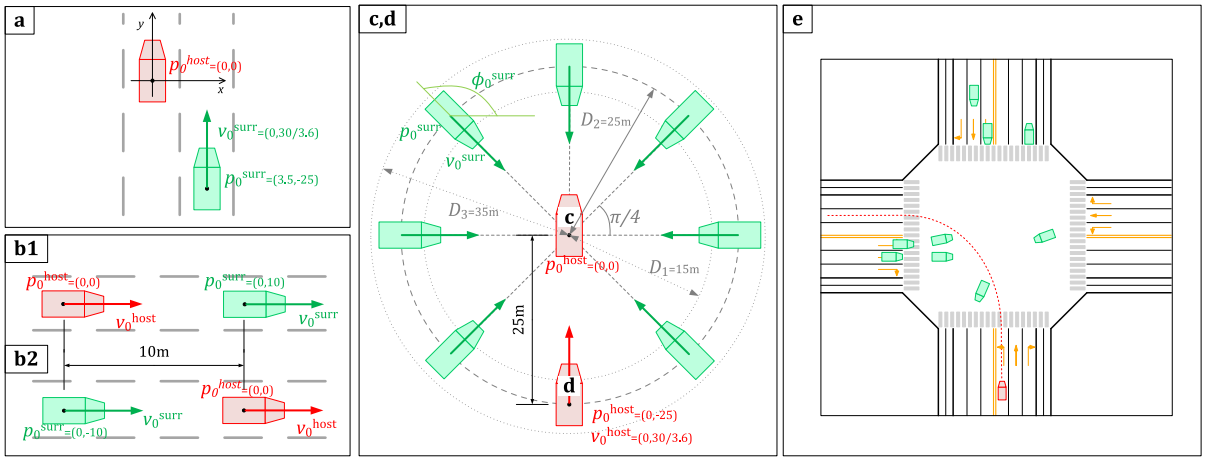

Fig. 6. Designs of case study situations

3 Results

3.1 Single Surrounding object

3.1.1 Side Pass

Fig. 6a shows the design of this driving situation, and the results are shown in Fig. 7.

Fig. 7a shows the predicted trajectories and corresponding risk values at {0.0, 1.8, 3.0, 4.2, 6.0} seconds and the overall risk curve during driving. Offsets are added to show the risk values in the prediction horizon clearly. As can be seen, PODAR increases with the vehicle approaching the host vehicle and nearly keep constant when the two vehicles are driving side-by-side, and then decreases quickly after the surrounding vehicle passes the host vehicle. This trend is consistent with human cognition.

Fig. 7b shows risk values in the prediction horizon. For the cases at driving times 0.0 and 1.8, PODAR_t increase first due to shortened distances to the host vehicle, as shown in Fig. 7c. The following decrease trends are attributed to the time attenuation, as shown in Fig. 7e. The maximum PODAR shown in the whole prediction horizon will be determined as the final PODAR at a specific driving time. Therefore, the final PODAR at driving times 0.0 and 1.8 are the PODAR values shown at their predictive timesteps $\mathrm{t} = 2.4$ and $t = 0.6$ (indicated by the gray dot lines in Fig. 7b), respectively. It is easy to know that the maximum PODAR corresponds to the scene that the surrounding vehicle arrives at position $\boldsymbol{p}^{\mathrm{surr}} = (3.5, -5)$, where the two vehicles have the shortest relative contour distance and start to drive side-by-side (see Fig. 7c). Consequently, the estimated PODAR stays at a high level until the parallel driving ends. These results are in line with common sense as well.

For the case at driving times 3.0, the host and surrounding vehicles drive side by side so that both the distance and the time attenuation coefficients are maximum at the current driving time. The risk value at present is determined as the final risk of the case at driving times 3.0. For the cases at driving times 4.2 and 6.0, the risk values are negative because their V_t are all negative during their corresponding prediction horizon, which means that the surrounding vehicle is driving away from the host vehicle and drivers will perceive low, or even no risk from it. Low risks also simulate peoples' attention mechanism, which can be seen in the test with multiple surrounding vehicles.

Fig. 7d shows the estimated damages during the prediction horizon. It is not surprising that the damages have downtrend because we used the inner products instead of relative speeds. The combined effect of damage, distance, and time attenuation leads to a good driving risk assessment performance. Time attenuation curves in Fig. 7e are the same among the five cases because it is only relative to the host vehicle's state.

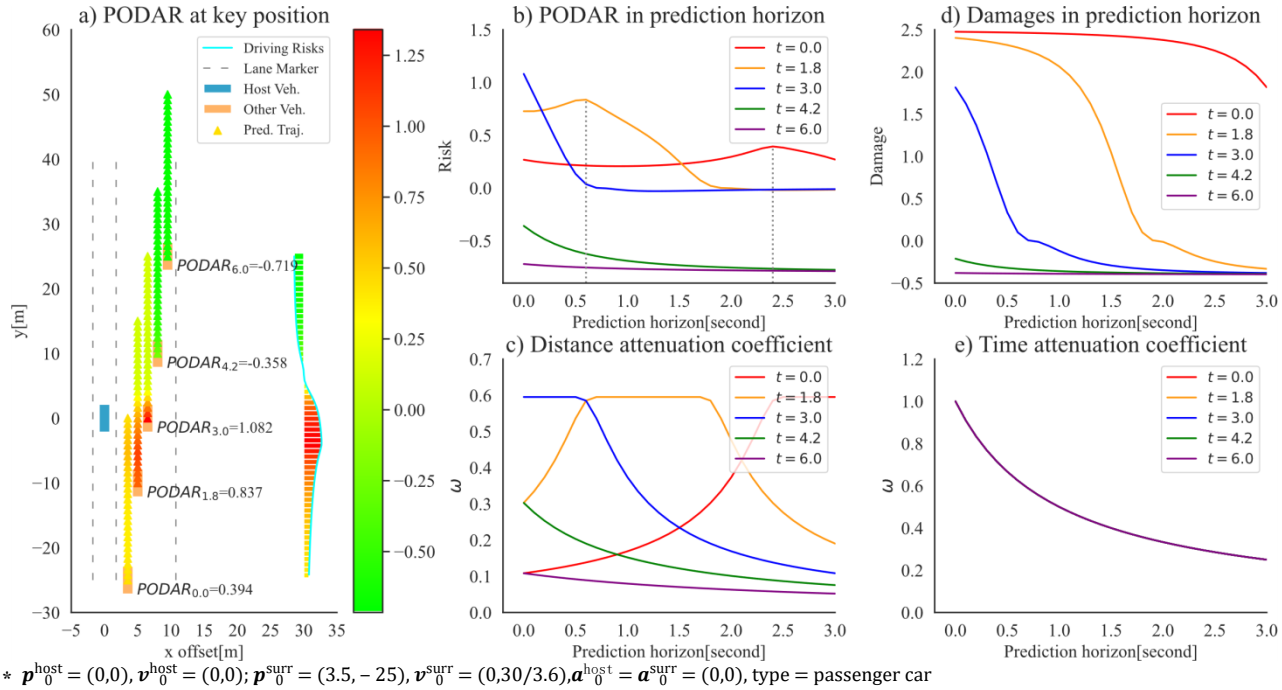

∗ $\boldsymbol{p}_0^{\text{host}} = (0,0)$, $\boldsymbol{v}_0^{\text{host}} = (0,0)$; $\boldsymbol{p}_0^{\text{surr}} = (3.5,-25)$, $\boldsymbol{v}_0^{\text{surr}} = (0,30/3.6)$, $\boldsymbol{a}_0^{\text{host}} = \boldsymbol{a}_0^{\text{surr}} = (0,0)$, type = passenger car

Fig. 7. Risks and intermediate variables of side pass scene.

3.1.2 Car-following

Vehicles drive at different speeds in front of or after the host vehicle

Fig. 6b shows the design of this driving situation. Fig. 8 shows the predictive results of the 8 car-following cases. Similarly, several offsets are added to have a clear presentation. Numbers in the white circle are the ranks of PODAR of different cases. It is not surprising that the vehicle coming from behind at a speed of 45*km/h* brings the highest risk because a rear-end collision will occur. Another vehicle driving 15*km/h* in front of the host vehicle will also cause a collision, but its risk is lower than the prementioned one because the velocity magnitude is smaller. Risks brought by the rest of the vehicles are also consistent with human cognition.

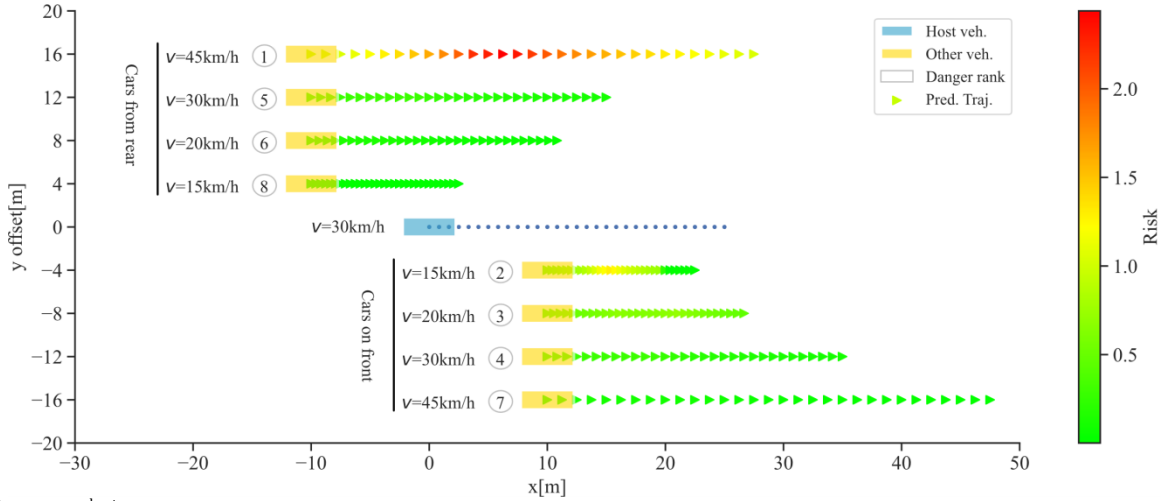

∗ $\boldsymbol{p}_0^{\text{host}} = (0,0)$, $\boldsymbol{v}_0^{\text{host}} = (30/3.6,0)$; $\boldsymbol{p}_0^{\text{surr}} = (D,0)$, $\boldsymbol{v}_0^{\text{surr}} = (V/3.6,0)$, $D \in \{-10,10\}m$, $V \in \{15,20,30,45\}km/h$,
$\boldsymbol{a}_0^{\text{host}} = \boldsymbol{a}_0^{\text{surr}} = (0,0)$, type = passenger car

Fig. 8. Risks of car-following scenes (same object type, instantaneous picture)

Car-following process

To better show the feasibility of the PODAR model, a typical car-following process with complex acceleration processes is designed, as shown in Fig. 9. The initial distance between the host and preceding vehicle is 20*m* (center to center distance). The initial speed values are 10*m/s* and 5*m/s* for the host and preceding vehicles. First, the host vehicle decelerates until its speed is lower than the preceding vehicle, and then both the two vehicles accelerate after cruising for a short time. There are two points where the host and the preceding vehicle have the same speed, marked by two black dash lines. This car-following process is common on urban roads.

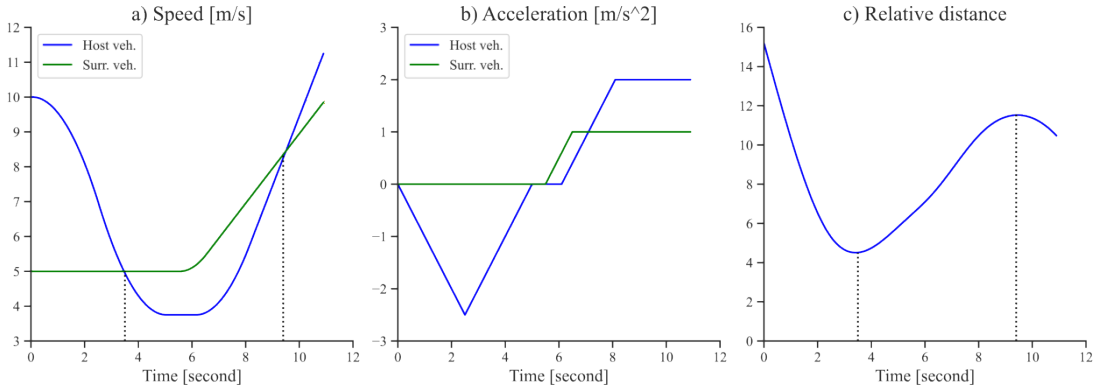

Fig. 9. Car-following scene design

Four risk measures, including PODAR, 1/TTC, DRAC, SF, and DRF are calculated, as shown in Fig. 10. Parameters used in SF calculation are customized according to paper [21][22], and parameters in DRF calculation refer to the literature [23], respectively. In general, TTC and DRAC are meaningless when the host vehicle's speed is lower than the front vehicle. However, their trend can also represent the risk changes (for DRAC, the opposite numbers between two black dash lines should be used due to the $(\Delta v)^2$ in its equation). Fig. 10b shows that 1/TTC and DRAC have a similar trend because they have similar forms.

The estimated risks by using these measures show a similar down-flat-rising trend. However, there are slight differences. Risks from 1/TTC, DRAC, and DRF all have a slight increase at the beginning because relative distance shortens fast than the decrease of relative speed, while PODAR and SF decrease continuously in the first phase. We suggest that PODAR and SF are more rational because the host vehicle's speed decreases and can avoid the collision.

As to the third phase, both the host and preceding vehicles speed up from driving time 6.0, PODAR and DRF soar up while the other three measures increase slowly. The reason is that PODAR introduces kinetic energy and DRF considers the host vehicle speed when getting the longitudinal height of Gaussian, while SF only considers the relative speed that changes slowly. It can be concluded that PODAR can obtain a similar risk trend to traditional and field-based measures but is better because it also has some features in reflecting human perceived risk like DRF.

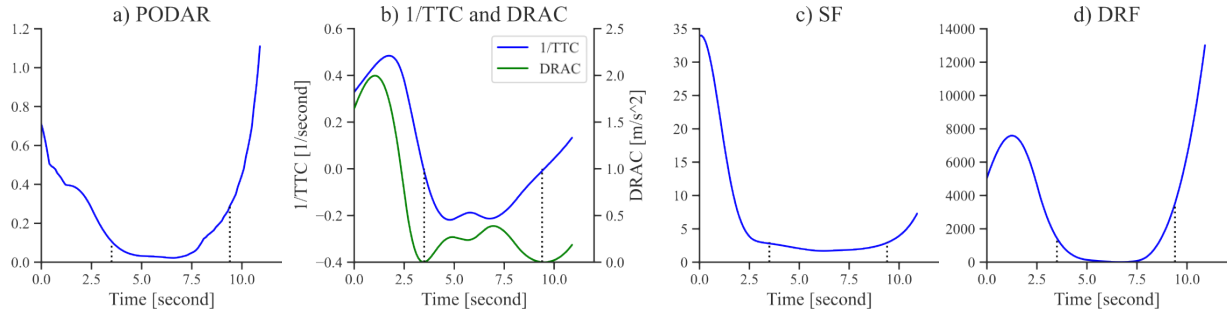

Fig. 10. Risks of the car-following scene (same object type, dynamic process)

3.1.3 Multi-angle Conflicts

Stationary host vehicle

Fig. 6c shows the design of this driving situation. Fig. 11 shows the results of multi-angle conflict scenes when the host vehicle stands still. Similarly, slight offsets are added for a clear presentation.

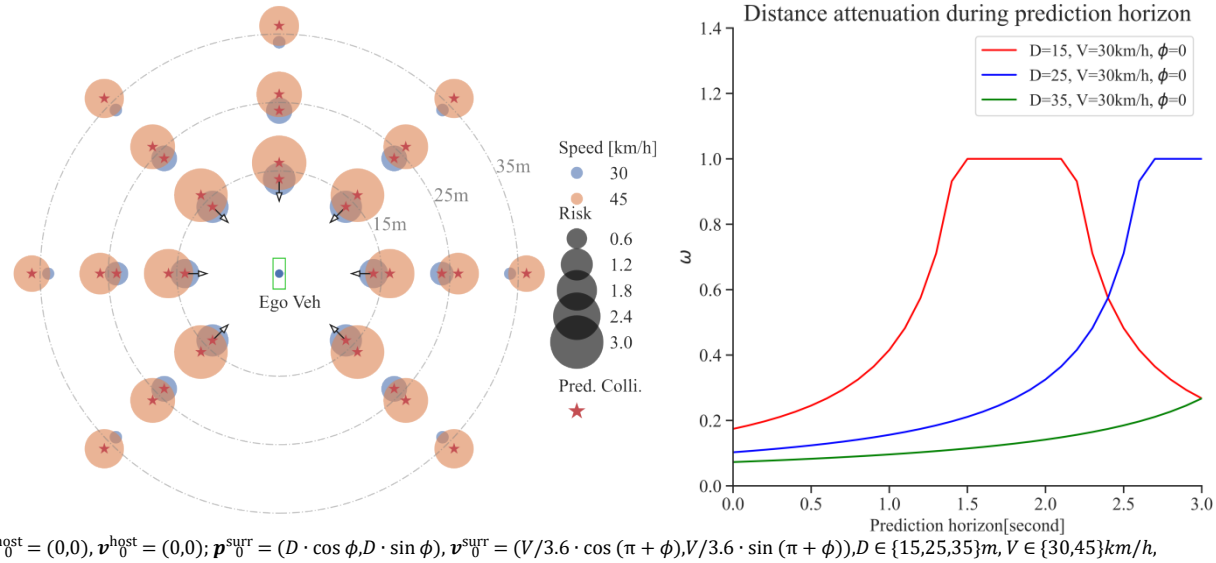

* $\boldsymbol{p}_0^{\text{host}} = (0,0), \boldsymbol{v}_0^{\text{host}} = (0,0); \boldsymbol{p}_0^{\text{surr}} = (D \cdot \cos\phi, D \cdot \sin\phi), \boldsymbol{v}_0^{\text{surr}} = (V/3.6 \cdot \cos(\pi + \phi), V/3.6 \cdot \sin(\pi + \phi)), D \in \{15,25,35\}m, V \in \{30,45\}km/h,$
$\phi \in \{-\frac{\pi}{4}, 0, \frac{\pi}{4}, \frac{\pi}{2}, \frac{3\pi}{4}, \pi, -\frac{3\pi}{4}\}, \boldsymbol{a}_0^{\text{host}} = \boldsymbol{a}_0^{\text{surr}} = (0,0)$, type = passenger car

Fig. 11. Risks of scenes having potential collisions when the host vehicle is stationary

Nearly all the surrounding vehicles will collide with the host vehicle during the future 3 seconds. Vehicles with the same speed and distance to the host vehicle have similar risks. It is because the host vehicle is stationary, so the relative velocity vector and the relative position vector have the same direction, resulting in the same inner product values. Vehicles with 30*km/h* bring fewer risks than vehicles with 45*km/h* due to the difference in potential collision damage. The risk variance between vehicles having different initial distances to the host vehicle is attributed to the distance attenuation, as shown in the right graph of Fig. 11. Potential damages from vehicles at 15*m* do not attenuate from $t = 1.5$ to $t = 2.1$ in the predictive horizon because the collision will occur during the time interval. Recalling that they have the same time attenuation curve, the risk of vehicles at 15*m* is higher than others. The results are consistent with TTC and SF results: when the host vehicle is stationary, the near the surrounding vehicles are, the higher the risks.

TTC uses a time-based measure to describe risks. However, as mentioned above, in the PODAR model, we have the same time attenuation curve, and the risk differences are brought by the distance changes, leading to similar risk ranks. TTC uses the relative speed so that all the collision scenes can be normalized to scenes in Fig. 11 from the view of the host vehicle reference system. Thus, TTC will have a similar interpretation by decoupling the spatial and temporal dimensions.

As to SF and DRF, one drawback is that they only concern either the surrounding object's states or the host vehicle's states. Therefore, they are able to perform well in the scenes with stationary host vehicles but will lead to different, even contrary, results compared with TTC when the host vehicle is traveling, as shown in the following case.

Moving host vehicle

Fig. 6d shows the design of this driving situation. Fig. 12 shows the results of multi-angle conflict scenes when the host vehicle moves, indicating some opposite conclusions to the above cases. Concerning vehicles with a speed of 45*km/h* and collision angle of ± 90 degrees, risks brought by vehicles at 35*m* are higher than those at 25*m* and 15*m*, except for the vehicles heading south. It is easy to understand that vehicles at 25*m* and 15*m* will pass the potential collision spots before the host vehicle arrives, while vehicles at 35*m* will exactly collide with the host vehicle. A similar performance can also be seen in the case where the vehicle at 25*m* with 30*km/h* has high risk than vehicles at 15*m*. Obviously, this result is consistent with PET. Details of the predicted risk values from the PODAR model can be seen in the right graph in Fig. 12. Although the vehicles at 25*m* with the speed of 45*km/h* have severe potential damage, the long distances to host vehicles lead to a stronger attenuation than the vehicles at 25*m* with the speed of 30*km/h*. The risk value can be used to alert the host vehicle to avoid the collision.

However, it is easy to imagine that SF and DRF will lead to contrary results that the vehicle at 15*m* brings the highest risk because they ignore the motion of the host and surrounding vehicles, missing the critical component of "Projection" in Situation Awareness theory. Therefore, these cases prove that the proposed PODAR model can cover the advantages of both TTC series measures and the SF.

Vehicles heading south have similar risk ranks to those in Fig. 11 because they will always collide with the host vehicle, so the nearer the surrounding vehicles, the higher the risks.

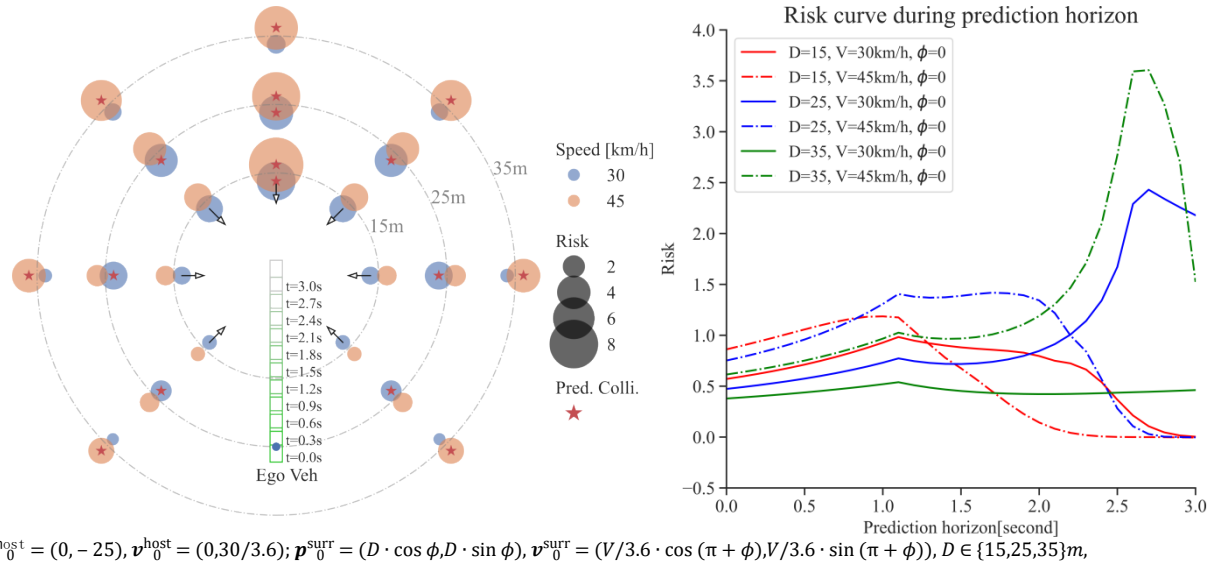

* $\boldsymbol{p}_0^{\text{host}} = (0, -25)$, $\boldsymbol{v}_0^{\text{host}} = (0, 30/3.6)$; $\boldsymbol{p}_0^{\text{surr}} = (D \cdot \cos\phi, D \cdot \sin\phi)$, $\boldsymbol{v}_0^{\text{surr}} = (V/3.6 \cdot \cos(\pi + \phi), V/3.6 \cdot \sin(\pi + \phi))$, $D \in \{15, 25, 35\}m$, $V \in \{30, 45\}km/h, \phi \in \{-\frac{\pi}{4}, 0, \frac{\pi}{4}, \frac{\pi}{2}, \frac{3\pi}{4}, \pi, -\frac{3\pi}{4}\}$, $\boldsymbol{a}_0^{\text{host}} = \boldsymbol{a}_0^{\text{surr}} = (0, 0)$, type = passenger car

Fig. 12. Risks of scenes having potential collisions when the host vehicle is traveling (same object type)

3.1.4 Differences in Objects Types

The following cases show the influence of object types on driving risks. A vast mass will result in a high driving risk, as shown in the left graph of Fig. 13, where trucks and passenger cars are tested. By multiplying a "sensitivity" factor to the actual mass of objects, the bicycles will bring higher risks than passenger cars due to a higher virtual mass, as shown in the right graph of Fig. 13, letting the host vehicle pay more attention to vulnerable traffic participants.

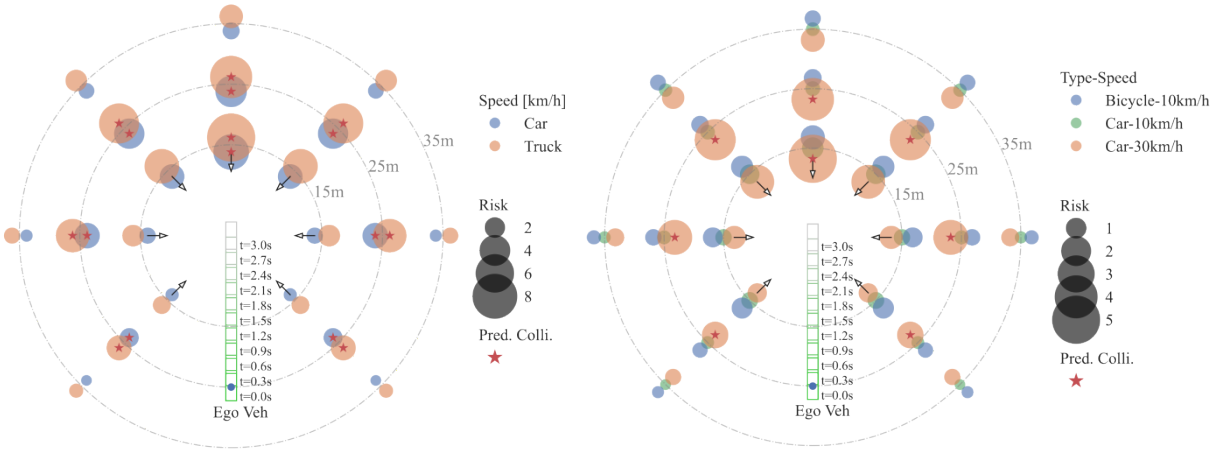

* $\boldsymbol{p}_0^{\text{host}} = (0, -25)$, $\boldsymbol{v}_0^{\text{host}} = (0, 30/3.6)$; $\boldsymbol{p}_0^{\text{surr}} = (D \cdot \cos\phi, D \cdot \sin\phi)$, $\boldsymbol{v}_0^{\text{surr}} = (V/3.6 \cdot \cos(\pi + \phi), V/3.6 \cdot \sin(\pi + \phi))$, $D \in \{15, 25, 30\}m$, $V \in \{10, 30, 45\}km/h, \phi \in \left\{-\frac{\pi}{4}, 0, \frac{\pi}{4}, \frac{\pi}{2}, \frac{3\pi}{4}, \pi, -\frac{3\pi}{4}\right\}$, $\boldsymbol{a}_0^{\text{host}} = \boldsymbol{a}_0^{\text{surr}} = (0, 0)$, type $\in$ {passenger car, truck, bycycle}

Fig. 13. Risks of scenes having potential collisions when the host vehicle is traveling (different object type)

3.2 Multi-Surrounding Vehicles in an Intersection

Fig. 6e shows the design of this driving situation. Fig. 14 plots twelve keyframes during a left-turn driving task on a standard unsignalized crossing. In this scenario, the host vehicle driving from the south approaches the left exit. Vehicles whose Manhattan distance to the host vehicle is less than $50m$ are considered in the driving risk assessment, represented by rectangles with blue edges. The filled colors represent the risks brought by the specific vehicles, where red means the highest, and green means the lowest. The risk values are also labeled on the right-top corner of the rectangle. The line in the left-bottom subgraph shows the risk changes during driving. If the line color becomes red, a potential collision is detected within the prediction horizon. A red dot on the line means an actual collision at that time.

At the simulation time of $77.9s$, the highest risk comes from vehicle#1, which drives from the opposite. After vehicle#1 passes the host vehicle, the highest risk comes from vehicle#2 from the north approach to the right exit ($78.7s$). However, our model determines that vehicle#2 will turn left and drive away from the host vehicle, so its risk decreases quickly, and then the highest risk comes from vehicle#3 ($79.9s$). Vehicle #3 continues to approach the host vehicle, but the risk decreases until $81.6s$ because the speeds of both vehicle#3 and the host vehicle continue to decrease, resulting in

a downtrend of estimated potential collision damage. In fact, the host vehicle entirely stops at 80.0*s*, then the risk increases as vehicle#3 approaches the host vehicle, and a collision occurs at 82.7*s*.

Meanwhile, vehicle#4 passes the host vehicle in the right lane, but its threat is lower than vehicle#3 because it has nearly the same driving direction as the host vehicle and does not cause a collision. Then the next threat comes from vehicle#5, which passes the host vehicle without collision. At 88.6*s*, risks from the other three vehicles are all lower than that from vehicle#7, so the risk value from vehicle#7 is chosen as the current risk. Vehicle #6 stops from 85.9*s* and starts to run at 90.3*s*, so the risk increases. Then it passes the host vehicle. The risk changes during the passing are consistent with the previous passing cases. As can be seen, the results from the proposed model are nearly like human cognition of the driving risk, even though there are many traffic participants with different driving courses.

If concerning changes in risk ranks of surrounding vehicles, it is interesting that the PODARs of surrounding vehicles at each time are similar to drivers' attention, leading to a human-like driving risk perception performance. With this feature, PODAR is anticipated to support the development of human-like planning algorithms, allowing self-driving drives like a human.

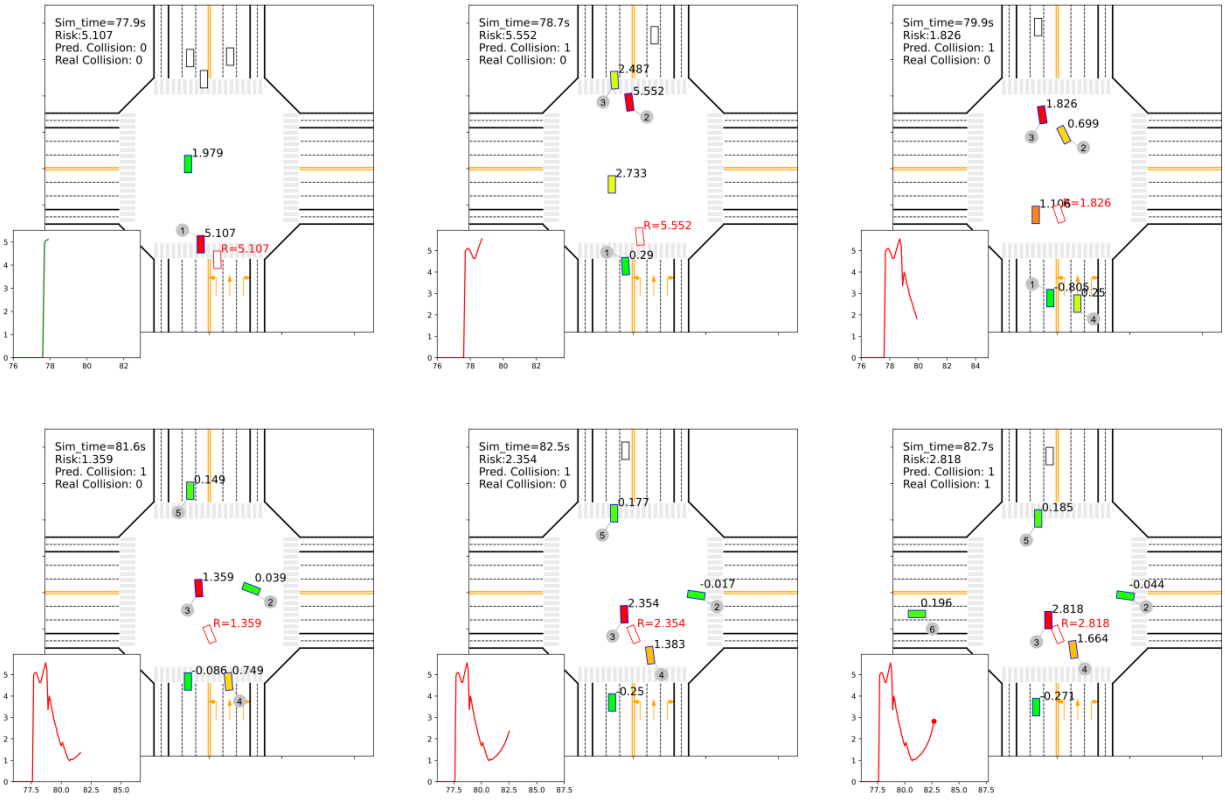

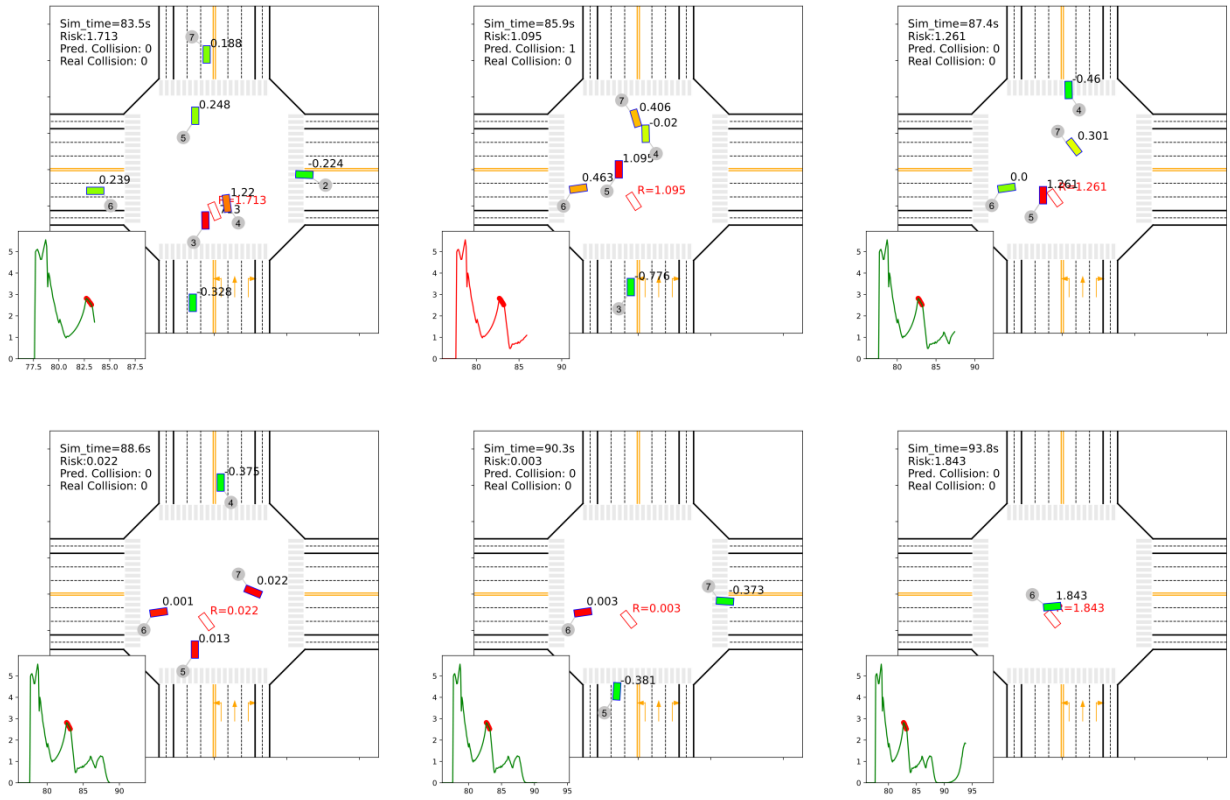

* The host vehicle: a rectangle with a red edge and white face;
* The surrounding vehicle in the risk assessment area: color-filled (red=high risk, green=low risk) rectangles with a blue edge.

Fig. 14. Risk changes during a left-turn task

4 Discussion

One significant contribution of our work is to illuminate the relationship between the driving risk concept and human situation awareness theory. Based on the relationship, a novel model with concise form and general scene availability, called PODAR, is proposed to estimate the driver's perceived risk. Different from probability in traditional field-based measures, PODAR uses two attenuation functions to describe the uncertainty by regarding the risk as to the threat of possible damage. This idea connects the risk values to damage values by a simple and intuitive interpretation that damage is the supremum of risk, endowing the risk a practical significance.

Generally, narrow time and space rooms will increase the possibility of damage becoming real, indicating that closer objects bring higher risk, as most of the results shown in the case study. However, due to the future dynamic, existed measures under some situations will lead to counterintuitive results. For example, representative scenes are the conflict-with-angle scenarios shown in Fig. 12, where DRF and SF are invalidated. Kolekar, the proposer of DRF, says in their paper [25] that DRF is inconclusive for 90-degree intersections. The illumination of the relationship between risk and SA theory provides an explanation that DRF only predicts the motion of the host vehicle while ignoring the motion of surrounding objects, leading to a low risk even though a collision will occur.

Also, the reason why TTC is popular with its straightforward forms can also be explained. TTC or DRAS has the advantage of containing a simple trajectory prediction in its model. If only concerning the happening of collision, i.e., setting goals as accident avoidance, TTC and DARS also obey the SA theory and especially have the "Projection" feature, which is regarded as a mark of a skilled expert but is neglected by SF and DRF. PODAR generalizes TTC, holding the conciseness features meanwhile.

The disadvantage of TTC-series measures that they are limited to car-following-similar driving situations, can also be explained. If we put TTC into the PODAR concept, TTC can be seen as one alternative for the attenuation functions, so that is just a particular case of PODAR. However, TTC only considers the collision moment, i.e., distance=0 at an arbitrary time, and does not consider the crash severity. Therefore, at least one potential collision spot is needed, which limits its scene adaptability. Similarly, DRAC, whose definition is $(\Delta v)^2/\Delta d$, can also be seen as one case of PODAR.

Besides, the introduction of trajectory prediction provides a path that allows autonomous vehicle planning algorithms to evaluate their planned trajectories stepwise. With this feature, more flexible and human-like trajectories can be generated.

There also are some issues to be solved in PODAR. Equation (1) uses a maximize function to simulate human attention, and Fig. 14 also shows expected results. However, it would lead to some jump-change points when the host and surrounding vehicle's motion changes rapidly. One potential improvement way is to use a weighted sum for each surrounding vehicle (maximize function can be seen as one particular case like Dirac functions).

Accurate trajectory prediction is essential for PODAR. Although the simple prediction model in Equation (11) performs well, uncertainty in the trajectory prediction needs more consideration, like introducing the multiple trajectories forecast and prediction with the considering road alignments.

Another issue is the relationship between PODAR and real damage when a collision occurs. It is generally thought that a collision, even a slight touch, will be riskier than a high-speed skittering. This will lead to a dilemma that the estimated risk of colliding should be higher than that shown in non-collision situations to meet the expectation of human cognition. Here, we slightly modify the initial distance of the dynamic car-following scene from 20m to 15m, and the corresponding results are shown in Fig. 15. As can be seen, there is a rear-end collision at 2.9 seconds, labeled as red dots. The estimated PODAR and SF do not show an expected high value because vehicle speed values are lower than other non-collision moments. However, PODAR provides a higher value before collision than that in Fig. 10 due to that it has detected collisions. SF and DRF also have similar results, while 1/TTC and DRAC, in this case, show a high value as expected. Two candidates that could solve this issue are i) combining the application of PODAR for non-collision risk estimation and 1/TTC or DRAC for collision detection and ii) adding a coefficient to damage estimation when there is predicted to have a collision, thus increasing the final risk without breaking the current framework.

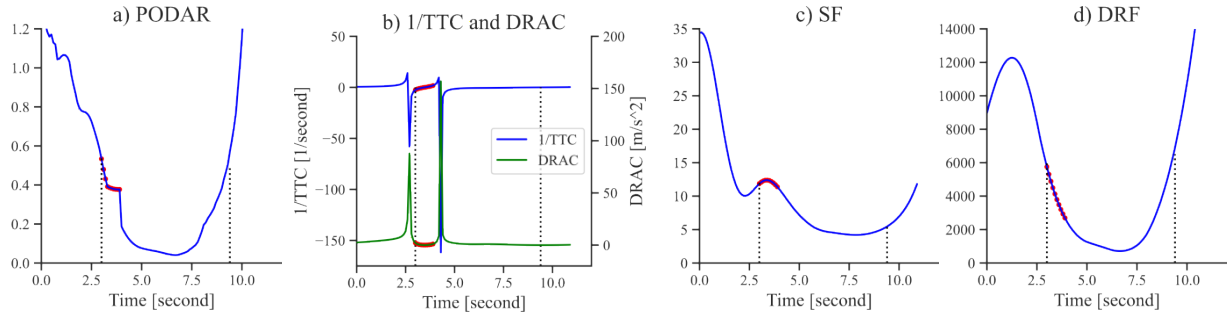

Fig. 15. Risks of the car-following scene with collision

Besides, TTC and DRAC are intuitionistic representations of potential collisions, while PODAR seems like an abstract concept to describe human cognition. We can take an analogy between the damage with vehicle repair fees or body treatment costs. High PODAR means high repair fees or treatment costs, and humans tend to avoid these economic costs. Broadly, the PODAR can also replace the potential damage with vehicle insurance fees when applying to autonomous driving development.

5 Conclusion

This paper introduces human situation awareness theory to the driving risk concept, and a novel model called PODAR used for driver's perceived risk estimation is proposed. PODAR considers the future dynamic of both the host vehicle and surrounding objects, where a damage model and two attenuation functions are used to simulate human risk perception. PODAR is well concise but effective, which is proved by the results under typical driving situations, including side pass, car-following, and conflict scenes. It is also feasible under general traffic scenarios with multiple surrounding road users and can even simulate the driver's attention during driving. Besides, the introduction of situation awareness also explains the advantages and disadvantages of existing driving risk measures.

6 Acknowledgement

This study is supported in part by the National Natural Science Foundation of China under No. 52102411 and No. U20A20334, and in part by the Tsinghua University-Didi Joint Research Center for Future Mobility.

References

[1] Urmson, C., 2008. Self-driving cars and the urban challenge. IEEE Intelligent Systems, 23(2), pp.66-68.

[2] Muhammad, K., Ullah, A., Lloret, J., Del Ser, J. and de Albuquerque, V.H.C., 2020. Deep learning for safe autonomous driving: Current challenges and future directions. IEEE Transactions on Intelligent Transportation Systems, 22(7), pp.4316-4336.

[3] Kolekar, S., Petermeijer, B., Boer, E., de Winter, J. and Abbink, D., 2021. A risk field-based metric correlates with driver's perceived risk in manual and automated driving: A test-track study. Transportation research part C: emerging technologies, 133, p.103428.

[4] Azevedo-Sa, H., Zhao, H., Esterwood, C., Yang, X.J., Tilbury, D.M. and Robert Jr, L.P., 2021. How internal and external risks affect the relationships between trust and driver behavior in automated driving systems. Transportation research part C: emerging technologies, 123, p.102973.

[5] ISO31000, "Ris management-principles and guidelines." International Organization for Standardization, 2018.

[6] Wikipedia, Risk, https://en.wikipedia.org/wiki/Risk, Access May 2022.
[7] Dowling, G.R., 1986. Perceived risk: the concept and its measurement. Psychology & Marketing, 3(3), pp.193-210.
[8] McNeil, A.J., Frey, R. and Embrechts, P., 2015. Quantitative risk management: concepts, techniques and tools-revised edition. Princeton university press.
[9] Carson, J.M., Elyasiani, E. and Mansur, I., 2008. Market risk, interest rate risk, and interdependencies in insurer stock returns: A system‐GARCH model. Journal of Risk and Insurance, 75(4), pp.873-891.
[10] Raymond, A.B., 1960. Consumer Behavior as Risk Taking. In Dynamic Marketing for a Changing World (pp. 389-398). American Marketing Association Chicago, Illinois.
[11] Endsley, M.R., 1988, October. Design and evaluation for situation awareness enhancement. In Proceedings of the Human Factors Society annual meeting (Vol. 32, No. 2, pp. 97-101). Sage CA: Los Angeles, CA: Sage Publications.
[12] Endsley, M.R., 2000. Theoretical underpinnings. Situation Aware Anal Measur, 1.
[13] Lee, D.N., 1976. A theory of visual control of braking based on information about time-to-collision. Perception, 5(4), pp.437-459.
[14] Minderhoud, M.M. and Bovy, P.H., 2001. Extended time-to-collision measures for road traffic safety assessment. Accident Analysis & Prevention, 33(1), pp.89-97.
[15] Archer, J., 2005. Indicators for traffic safety assessment and prediction and their application in micro-simulation modelling: A study of urban and suburban intersections (Doctoral dissertation, KTH).
[16] Wang, C. and Stamatiadis, N., 2013. Surrogate safety measure for simulation-based conflict study. Transportation research record, 2386(1), pp.72-80.
[17] Allen, B.L., Shin, B.T. and Cooper, P.J., 1978. Analysis of traffic conflicts and collisions (No. HS-025 846).
[18] Cooper, P.J., 1984. Experience with traffic conflicts in Canada with emphasis on “post encroachment time” techniques. In International calibration study of traffic conflict techniques (pp. 75-96). Springer, Berlin, Heidelberg.
[19] Gibson, J.J., Crooks, L.E., 1938. A theoretical field-analysis of automobile-driving. Am. J. Psychol. 51 (3), 453–471.
[20] Godthelp, H., 1986. Vehicle control during curve driving. Hum. Factors 28 (2), 211–221.
[21] Wang, J., Wu, J., Li, Y. and Li, K., 2014, October. The concept and modeling of driving safety field based on driver-vehicle-road interactions. In 17th International IEEE Conference on Intelligent Transportation Systems (ITSC) (pp. 974-981). IEEE.
[22] Wang, J., Wu, J., Qin, H. and Li, K., 2015, October. Modified driving safety field theory and its application to collision warning algorithm in complex traffic environments. In 22nd ITS World Congress, Bordeaux (pp. 5-9).
[23] Kolekar, S., de Winter, J. and Abbink, D., 2020. Human-like driving behaviour emerges from a risk-based driver model. Nature Communications, 11(1), pp.1-13.
[24] Kolekar, S., de Winter, J. and Abbink, D., 2020. Which parts of the road guide obstacle avoidance? Quantifying the driver’s risk field. Applied Ergonomics, 89, p.103196.
[25] Kolekar, S., Petermeijer, B., Boer, E., de Winter, J. and Abbink, D., 2021. A risk field-based metric correlates with driver’s perceived risk in manual and automated driving: A test-track study. Transportation research part C: emerging technologies, 133, p.103428.
[26] Xu, M., Song, Y., Wang, J., Qiao, M., Huo, L. and Wang, Z., 2018. Predicting head movement in panoramic video: A deep reinforcement learning approach. IEEE transactions on pattern analysis and machine intelligence, 41(11), pp.2693-2708.
[27] Xia, Y., Zhang, D., Kim, J., Nakayama, K., Zipser, K. and Whitney, D., 2018, December. Predicting driver attention in critical situations. In Asian conference on computer vision (pp. 658-674). Springer, Cham.
[28] Palazzi, A., Abati, D., Solera, F. and Cucchiara, R., 2018. Predicting the Driver’s Focus of Attention: the DR (eye) VE Project. IEEE transactions on pattern analysis and machine intelligence, 41(7), pp.1720-1733.
[29] Baee, S., Pakdamanian, E., Kim, I., Feng, L., Ordonez, V. and Barnes, L., 2021. Medirl: Predicting the visual attention of drivers via maximum entropy deep inverse reinforcement learning. In Proceedings of the IEEE/CVF International Conference on Computer Vision (pp. 13178-13188).
[30] Zheng, X., Zhang, D., Gao, H., Zhao, Z., Huang, H. and Wang, J., 2018. A novel framework for road traffic risk assessment with HMM-based prediction model. Sensors, 18(12), p.4313.
[31] Ozbay, K., Yang, H., Bartin, B. and Mudigonda, S., 2008. Derivation and validation of new simulation-based surrogate safety measure. Transportation research record, 2083(1), pp.105-113.
[32] Gettman, D. and Head, L., 2003. Surrogate safety measures from traffic simulation models. Transportation Research Record, 1840(1), pp.104-115.
[33] Shelby, S.G., 2011, January. Delta-V as a measure of traffic conflict severity. In 3rd International Conference on Road Safety and Simulati. September (pp. 14-16).
[34] Jurecki, R.S. and Stańczyk, T.L., 2014. Driver reaction time to lateral entering pedestrian in a simulated crash traffic situation. Transportation research part F: traffic psychology and behaviour, 27, pp.22-36.
[35] Wikipedia, Truck, https://en.wikipedia.org/wiki/Truck, Access May 2022.
[36] Walpole, S.C., Prieto-Merino, D., Edwards, P., Cleland, J., Stevens, G. and Roberts, I., 2012. The weight of nations: an estimation of adult human biomass. BMC public health, 12(1), pp.1-6.
[37] How much does a car weigh? https://mechanicbase.com/cars/car-weight/, Access May 2022.
[38] Gao, J., Sun, C., Zhao, H., Shen, Y., Anguelov, D., Li, C. and Schmid, C., 2020. Vectornet: Encoding hd maps and agent dynamics from vectorized representation. In Proceedings of the IEEE/CVF Conference on Computer Vision and Pattern Recognition (pp. 11525-11533).
[39] Phan-Minh, T., Grigore, E.C., Boulton, F.A., Beijbom, O. and Wolff, E.M., 2020. Covernet: Multimodal behavior prediction using trajectory sets. In Proceedings of the IEEE/CVF Conference on Computer Vision and Pattern Recognition (pp. 14074-14083).
[40] Deo, N. and Trivedi, M.M., 2018, June. Multi-modal trajectory prediction of surrounding vehicles with maneuver based lstms. In 2018 IEEE Intelligent Vehicles Symposium (IV) (pp. 1179-1184). IEEE.

[41] Schöller, C., Aravantinos, V., Lay, F. and Knoll, A., 2020. What the constant velocity model can teach us about pedestrian motion prediction. IEEE Robotics and Automation Letters, 5(2), pp.1696-1703.
[42] Lopez, P.A., Behrisch, M., Bieker-Walz, L., Erdmann, J., Flötteröd, Y.P., Hilbrich, R., Lücken, L., Rummel, J., Wagner, P. and Wießner, E., 2018, November. Microscopic traffic simulation using sumo. In 2018 21st international conference on intelligent transportation systems (ITSC) (pp. 2575-2582). IEEE.